Supplementary Material: Observing information backflow from controllable non-Markovian multi-channels in diamond

Ya-Nan Lu,[1,2,*] Yu-Ran Zhang,[3,*] Gang-Qin Liu,[1,4,†] Franco Nori,[3,5] Heng Fan,[1,4,6,‡] and Xin-Yu Pan[1,4,6,§]

[1]*Institute of Physics, Chinese Academy of Sciences, Beijing 100190, China*
[2]*School of Physical Sciences, University of Chinese Academy of Sciences, Beijing 100049, China*
[3]*Theoretical Quantum Physics Laboratory, RIKEN Cluster for Pioneering Research, Wako-shi, Saitama 351-0198, Japan*
[4]*Songshan Lake Materials Laboratory, Dongguan, Guangdong 523808, China*
[5]*Physics Department, University of Michigan, Ann Arbor, Michigan 48109-1040, USA*
[6]*CAS Center of Excellence in Topological Quantum Computation, Beijing 100190, China*

I. THEORETICAL DERIVATION

A. QFI flow and non-Markovianity

Considering a mixed state $\rho = \sum_j \lambda_j |j\rangle\langle j|$, with $\langle i|j\rangle = \delta_{ij}$ and a generator $\hat{\mathcal{O}}$, the quantum Fisher information (QFI) of a state $\rho(\theta) = \exp(-i\theta\hat{\mathcal{O}})\rho\exp(-i\theta\hat{\mathcal{O}})$ with respect to a parameter θ can be written as [1]

$$\mathcal{Q} = 2\sum_{\lambda_i+\lambda_j\neq 0}\frac{(\lambda_i-\lambda_j)^2}{\lambda_i+\lambda_j}|\langle i|\hat{\mathcal{O}}|j\rangle|^2. \tag{S1}$$

For a single qubit, any state can be expressed as

$$\rho = \mathbb{I}/2 + \sum_{\alpha=x,y,z} s_\alpha\,\hat{\sigma}_\alpha/2, \tag{S2}$$

with $\boldsymbol{r} = [s_x,\ s_y,\ s_z]$ being the Bloch vector and $r \equiv (s_x^2+s_y^2+s_z^2)^{\frac{1}{2}}$ being the Bloch length. The QFI with respect to the generator $\hat{\mathcal{O}} = \hat{\sigma}_z/2$ can be calculated as $\mathcal{Q} = r^2 - s_z^2$. For a qubit state with $\boldsymbol{s} = [1,\ 0,\ 0]$, its QFI can be calculated to be 1. The QFI plays a central role in quantum metrology and multipartite entanglement witness [2–4], which is also sufficient for measuring non-Markovianity [5].

We then consider a quantum process, described by a time-local master equation [6, 7]

$$\frac{\partial\rho}{\partial t} = -i[\hat{H},\rho] + \sum_j \gamma_j\left(\hat{A}_j\rho\hat{A}_j^\dagger - \{\hat{A}_j^\dagger\hat{A}_j,\rho\}/2\right), \tag{S3}$$

where $\hat{H}$ is the Hamiltonian for the open system without coupling to the bath, $\gamma_j(t)$ is the time-dependent decay rate, and $\hat{A}_j(t)$ is the time-dependent Lindblad operator. The QFI flow of the quantum open system can be divided into different subchannels as [5]

$$\mathcal{I} \equiv \partial\mathcal{Q}/\partial t = \sum_j \mathcal{I}_j, \tag{S4}$$

with

$$\mathcal{I}_j = \gamma_j(t)\mathcal{J}_j, \tag{S5}$$

and $\mathcal{J}_j \leq 0$. Therefore, the existence of any positive QFI subflow characterizes a quantum non-Markovian process based on the completely positive divisibility [6].

B. Measure of non-Markovianity via QFI subflows

From Eq. (4) in the main text, the non-Markovianity can be witnessed by the sum of time integrals of all inward QFI subflows. When $\phi_1 = \phi_2 = \pi/2$, QFI subflows $\mathcal{I}_{\rm n}(t)$, $\mathcal{I}_{\rm c}(t)$ and $\mathcal{I}_{\rm R}(t)$ can be calculated from QFI with different parameters: $\mathcal{Q}_{\rm R} \equiv \mathcal{Q}(t,0,0)$, $\mathcal{Q}_{\rm nR} \equiv \mathcal{Q}(t,0,\frac{\pi}{2})$, and $\mathcal{Q}_{\rm cR} \equiv \mathcal{Q}(t,0,\frac{\pi}{2})$, which can be expressed, with $\dot{\mathcal{Q}} \equiv \partial\mathcal{Q}/\partial t$, as

$$\begin{aligned}
\mathcal{I}_{\rm n} &= (\dot{\mathcal{Q}}_{\rm nR} - \mathcal{Q}_{\rm nR}\dot{\mathcal{Q}}_{\rm R}/\mathcal{Q}_{\rm R})\mathcal{Q}_{\rm cR}/\mathcal{Q}_{\rm R},\\
\mathcal{I}_{\rm c} &= (\dot{\mathcal{Q}}_{\rm cR} - \mathcal{Q}_{\rm cR}\dot{\mathcal{Q}}_{\rm R}/\mathcal{Q}_{\rm R})\mathcal{Q}_{\rm nR}/\mathcal{Q}_{\rm R},\\
\mathcal{I}_{\rm R} &= \mathcal{Q}_{\rm cR}\mathcal{Q}_{\rm nR}\dot{\mathcal{Q}}_{\rm R}/\mathcal{Q}_{\rm R}^2.
\end{aligned} \tag{S6}$$

II. EXPERIMENTAL DETAILS

In this section, we describe the experimental setup, sample information, spin coherence, and state tomography techniques in detail. Then we further explain the envelope of QFI induced by nuclear spin bath.

A. Setup and sample

Our experiments are performed under ambient conditions on a high-purity bulk diamond (Element Six, with N concentration < 5 p.p.b., and natural abundance of ^{13}C isotopes). The NV center is located 10 μm below the diamond surface. To enhance the photon collection efficiency of the NV center, solid immersion lenses (SILs) are etched on the diamond surface [8]. The photon detection rate is 450 kcps, when the laser (532 nm) excitation power is 240 μW.

We use optically detected magnetic resonance (ODMR) to detect nuclear spins, which are strongly coupled to the NV electron spin. From the continuous-wave ODMR spectrum under a small magnetic field $B \simeq 40$ Gauss [see Fig. S1(a)

* These authors contributed equally to this work.
† gqliu@iphy.ac.cn
‡ hfan@iphy.ac.cn
§ xypan@aphy.iphy.ac.cn

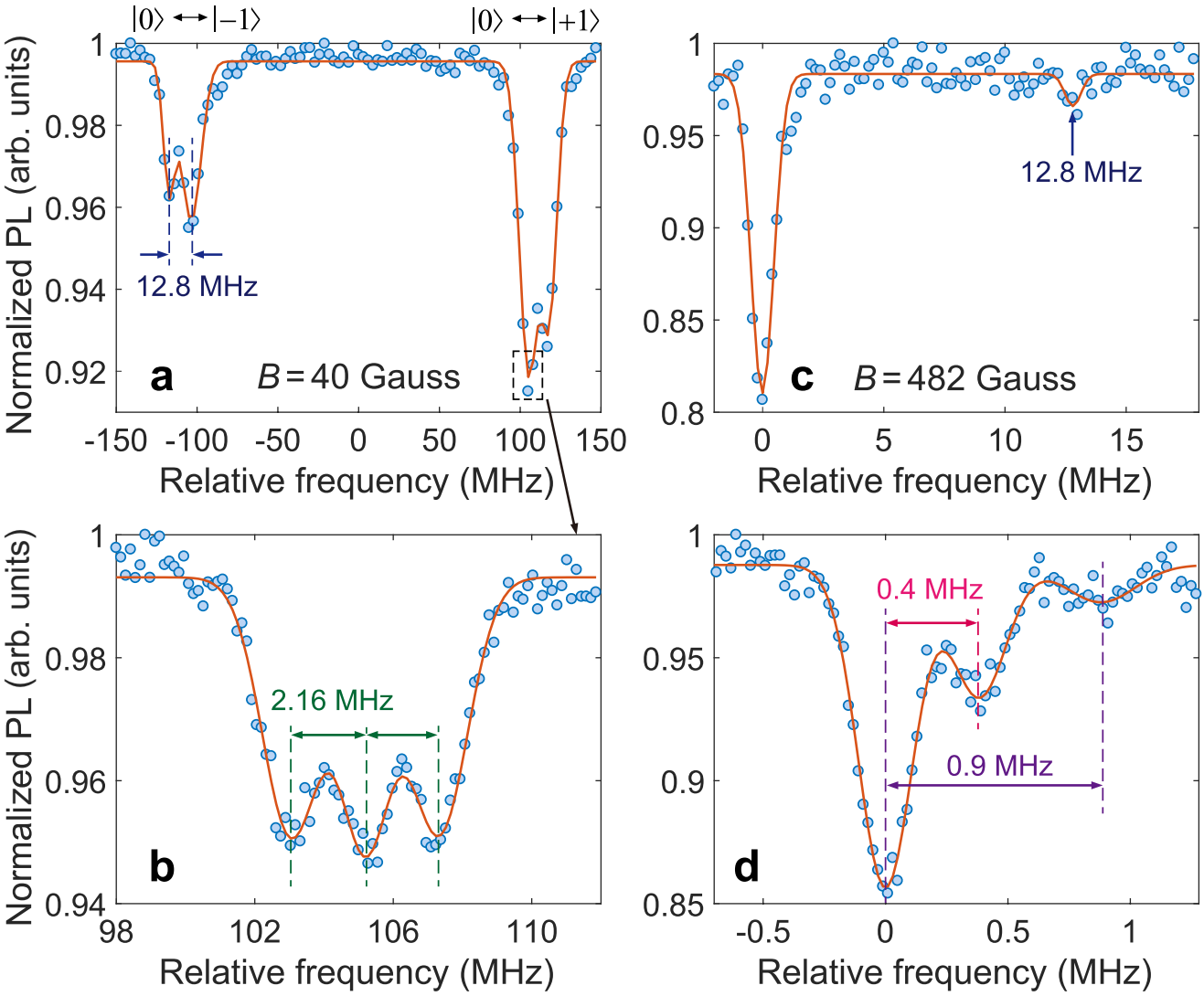

FIG. S1. Optically detected magnetic resonance (ODMR) spectra of the multi-qubit system. (a,b) Continuous-wave ODMR spectra under a small magnetic field with $B = 40$ Gauss (frequency is relative to 2,870 MHz). The 2.16 MHz and 12.8 MHz splittings are induced by the ^{14}N nuclear spin and the nearby ^{13}C nuclear spin, respectively. (c,d) Pulsed-ODMR spectra under a magnetic field with $B = 482$ Gauss (frequency is relative to 1,518 MHz). Both the host ^{14}N nuclear spin and the 12.8 MHz ^{13}C nuclear spin are polarized due to ESLAC, and two other nuclear spins (0.9 MHz and 0.4 MHz) is also resolved.

and S1(b)], the host ^{14}N nuclear spin and the nearby ^{13}C nuclear spin with 12.8 MHz coupling strength are identified [9]. To identify the nuclear spin with a weaker coupling strength, the external magnetic field is tuned to 482 Gauss (along the quantization axis of the NV center), and both the host ^{14}N and the 12.8 MHz ^{13}C nuclear spins can be polarized by a short laser pulse. We then measure the pulsed-ODMR spectra of the NV center [see Fig. S1(c)]. By reducing the microwave (MW) power, two other ^{13}C nuclear spins are resolved [see FIG. S1(d)]. The hyperfine splittings caused by these two ^{13}C nuclear spins are 0.9 MHz and 0.4 MHz, respectively. These two nuclear spins are partially polarized by the laser pumping [see Fig. S1(d)], which is consistent with the literature results [10]. In our experiments, the 12.8 MHz ^{13}C nuclear spin and the ^{14}N nuclear spin are taken as fully controllable decoherence channels, while the other nearby weakly-coupled ^{13}C nuclear spins behave as uncontrollable decoherence channels.

B. Relaxation and coherence of the NV electron spin

The electron spin and nuclear spins are manipulated by the resonant MW and radiofrequency (RF) pulses. Figure S2(a) shows a typical Rabi oscillation signal of the NV electron spin, with Rabi frequency 23.8 MHz. Figure S2(b) shows the Ramsey oscillation from a deliberate MW detuning (2 MHz) and the beating between different transitions, according to the state of the 0.4 MHz ^{13}C nuclear spin. By fitting the Ramsey signal, we obtain the dephasing time of this NV center as $T_{2e}^{\star} \approx 2.9 \pm 0.1$ μs, which is limited by thermal fluctuations

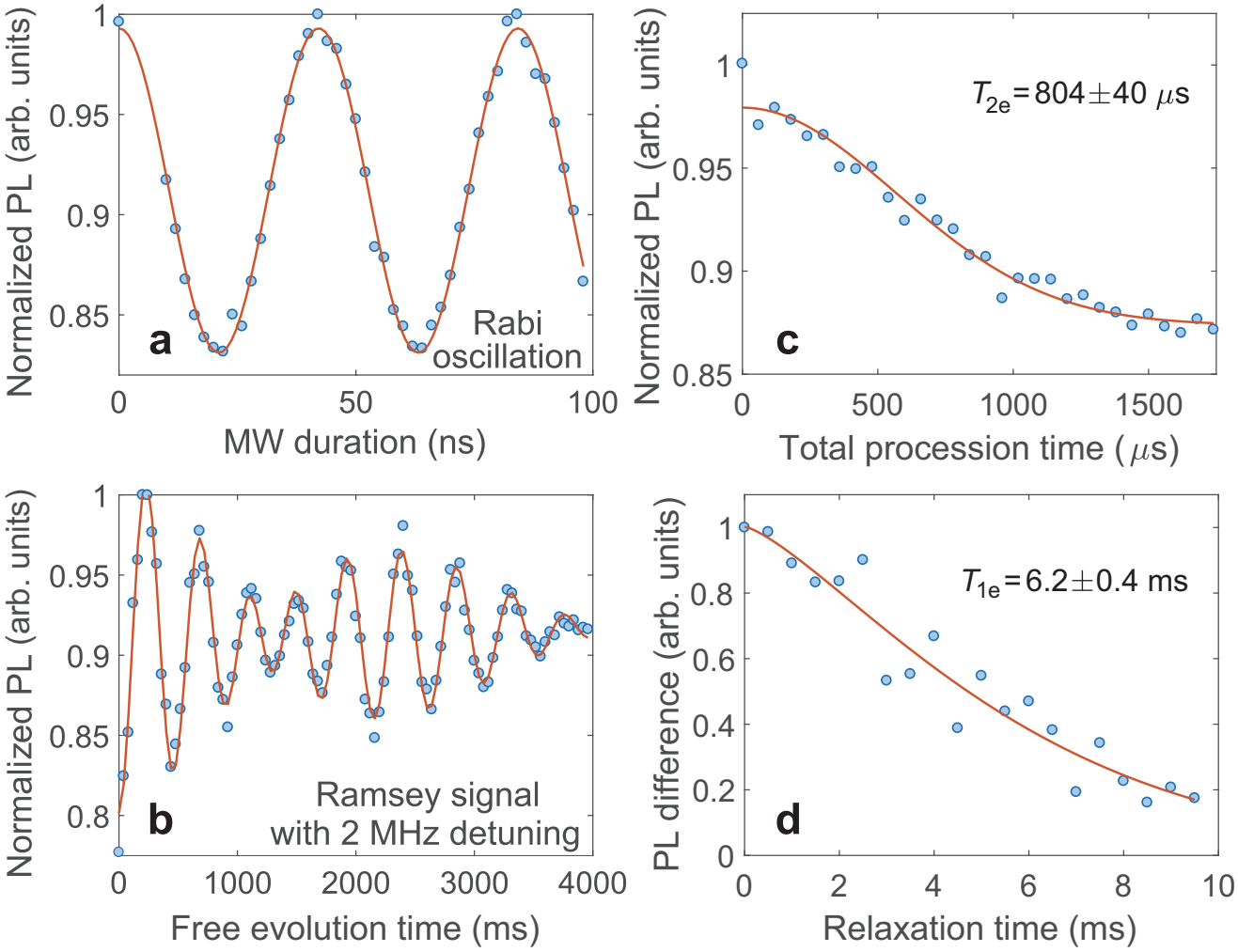

FIG. S2. Spin relaxation, decoherence and dephasing of the NV electron spin. (a) The Rabi oscillation and (b) the free induction decay (FID) of the NV electron spin (with a 2 MHz detuning). The dephasing time of the NV electron spin is $T_{2e}^{*} \simeq 2.9 \pm 0.1$ μs. (c) Spin echo (Hahn echo) signal. The coherence time of the NV electron spin is $T_{2e} = 804 \pm 40$ μs, which is determined by the evolution of the surrounding nuclear spin bath. (d) Spin relaxation signal, which gives the relaxation time of $T_{1e} = 6.2 \pm 0.4$ ms. In this high-purity diamond, the spin relaxation mechanism is the intrinsic spin-phonon interaction at room temperature.

of the nuclear spin bath. Figure S2(c) presents the spin echo (Hahn echo) signal of this NV center. As thermal fluctuations from the spin bath are canceled out by the flip pulse of the echo sequence, the spin coherence time of $T_{2e} = 804 \pm 40$ μs is obtained. The coherence time of the NV electron spin can be further prolonged with dynamical decoupling sequences. Figure S2(d) shows the spin relaxation signal of this NV center, which gives $T_{1e} = 6.2 \pm 0.4$ ms. In the room-temperature experiments with the high-purity diamond sample, the dominating spin relaxation mechanism is the intrinsic coupling between the NV spin and phonons [11]. The NV spin relaxation data is measured with a differential scheme. For each time interval, the $m_s = 0$ and $m_s = -1$ states are prepared and measured sequentially, and the fluorescence intensity difference between these two states is taken as the spin relaxation signal. This differential scheme excludes counts noise that are not related to the spin signal (e.g., charge fluctuations).

C. Coherence of the nearby nuclear spins

Ramsey oscillations of the two nearby nuclear spins are shown in Fig. S3. For the host ^{14}N nuclear spin, the dephasing time T_{2n}^{*} is 8.6 ± 2.4 (5.5 ± 1.9) ms, when the NV electron spin is at the $m_s = 0$ ($m_s = -1$) state. These values are close to the longitudinal relaxation time of the NV electron spin [see Fig. S2(d)], which is consistent with the fact that a single flip of the NV electron spin will give a random phase to the nuclear spin [12, 13]. To fit the experimental data, an exponential decay function with both the nuclear spin dephasing time (T_{2n}^{*}) and electron spin relaxation time [T_{1e}, extracted from Fig. S2(d) and fixed] is used:

$$\frac{1}{2}\left[1+\cos(\delta t)\exp\left(-\frac{t}{T_{2n}^{*}}\right)\right]\exp\left(-\frac{t}{T_{1e}}\right), \qquad \text{(S7)}$$

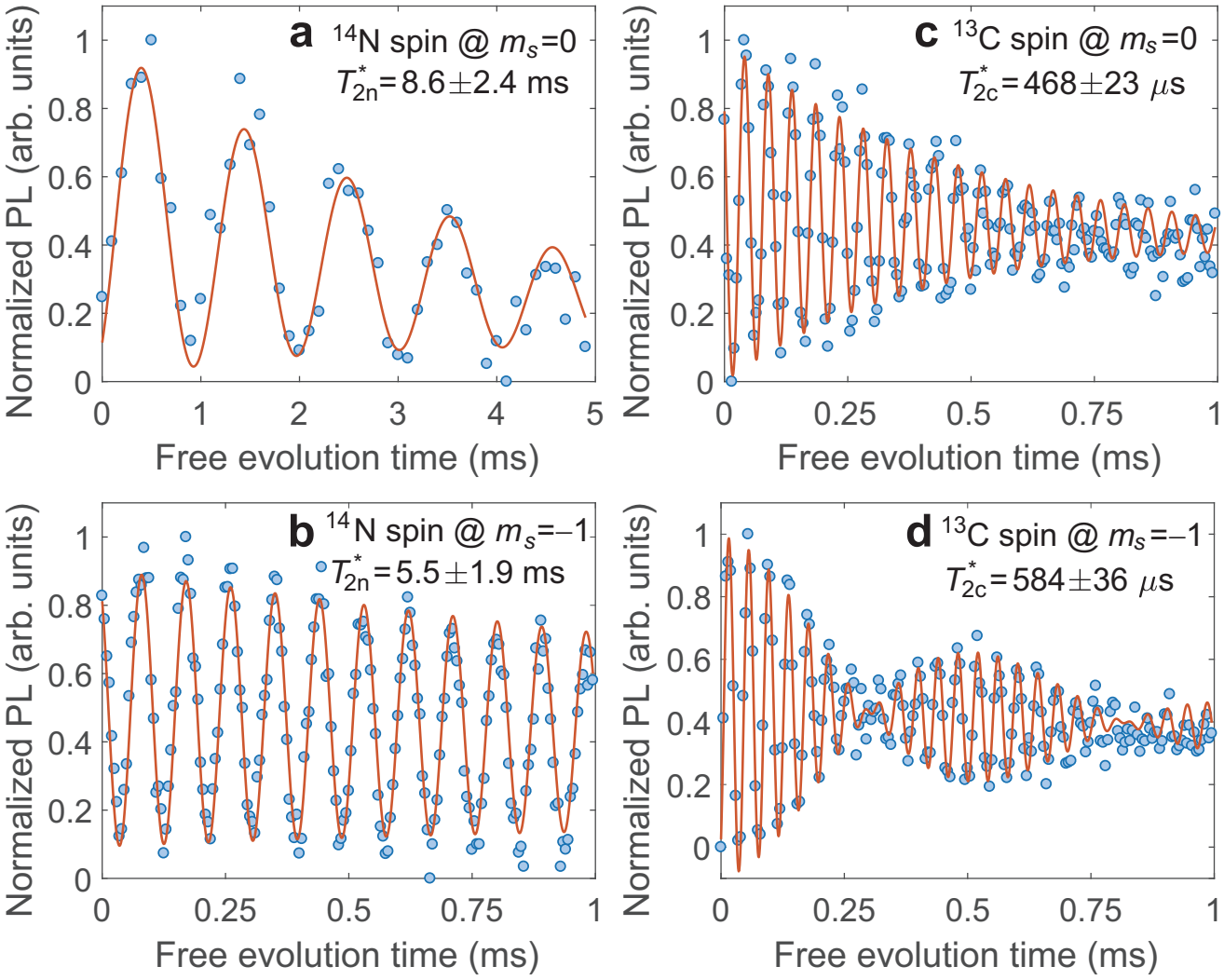

FIG. S3. Coherence of the nearby nuclear spins. (a–b) Free induction decay (FID) of the host ^{14}N nuclear spin, when the NV electron spin is prepared at (a) the $m_s = 0$ state and (b) the $m_s = -1$ state. The nuclear spin state is mapped onto the NV electron spin and then read out optically. The dephasing time of the ^{14}N nuclear spin is $T_{2n}^* = 8.6 \pm 2.4$ (5.5 ± 1.9) ms for the NV $m_s = 0$ ($m_s = -1$) state. The envelope decay is attributed to the electron spin relaxation process. (c–d) FID of the 12.8 MHz ^{13}C nuclear spin, when the NV electron spin is prepared at (c) the $m_s = 0$ state and (d) the $m_s = -1$ state. The dephasing time of the ^{13}C nuclear spin is $T_{2c}^* \simeq 0.5$ ms. The fast dephasing behavior may be induced by its interaction to other nearby nuclear spins. The beating in (d) gives a coupling strength of about 2 kHz. Another possible reason is the enhancement of the gyromagnetic ratio by the NV electron spin, as this nuclear spin is close to the center.

where δ is the detuning between the nuclear spin resonant frequency and the frequency of the applied RF pulses.

For the 12.8 MHz coupling ^{13}C nuclear spin, the dephasing time T_{2c}^* is 468 ± 23 (584 ± 36) μs, when the NV electron spin is at the $m_s = 0$ ($m_s = -1$) state, as shown in Fig. S3(c,d). This dephasing time is short as compared to the value of the ^{14}N nuclear spin. The about 3 times gyromagnetic ratio difference between the ^{13}C (1.071 kHz/Gauss) and ^{14}N (0.308 kHz/Gauss) nuclear spins is insufficient to interpret the about 10 times difference of the measured T_2^*. Other possible mechanisms of the fast nuclear spin dephasing include the enhancement of the gyromagnetic ratio by the NV electron spin, or interaction with other surrounding ^{13}C nuclear spins. The beating in Fig. S3(d) indicates that the 12.8 MHz ^{13}C nuclear spin is coupled to another nuclear spin, with a coupling strength of about 2 kHz. Meanwhile, a longer dephasing time ($T_2^* = 800$ μs) is observed for another ^{13}C nuclear spin with a weaker coupling to the same NV electron spin [0.9 MHz, see Fig. S1(d) for its ODMR spectrum].

D. State tomography

The sequence to implement the single-qubit state tomography can be divided into three parts: (i) Directly collect florescence photon counts L_z; (ii) prepare the state, apply a $\frac{\pi}{2}$ MW pulse along the x-axis, and then collect the florescence photon counts L_y; (iii) prepare the state, apply a $\frac{\pi}{2}$ MW pulse along

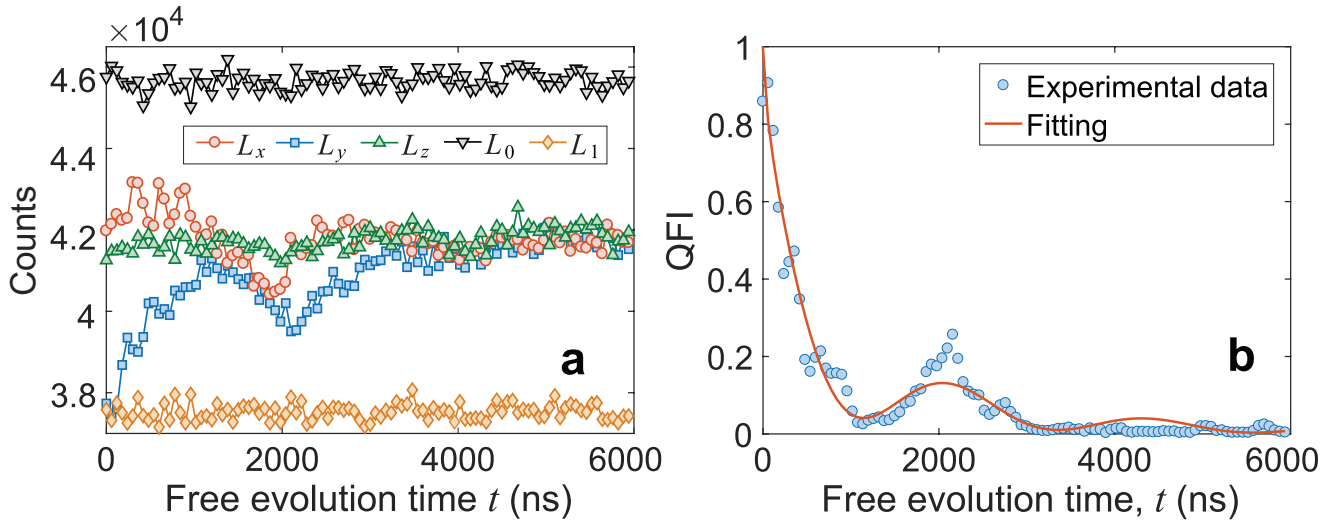

FIG. S4. Long-time QFI of the electron spin coupled to the uncontrolled spin bath. (a) Measured florescence photon counts as functions of the free evolution time. (b) QFI of the electron qubit as a function of the evolution time, where the oscillation is induced by the nearby partially polarized 0.4 MHz ^{13}C nuclear spin.

the y-axis, and then collect the florescence photon counts L_x. In addition, we collect the florescence photon counts L_0 in the bright state ($m_s = 0$), and L_1 in the dark state ($m_s = -1$), as references to normalize the florescence signal. With the signals on different bases, we can reconstruct the state by calculating the Bloch vector $\boldsymbol{r} = [s_x,\ s_y,\ s_z]$ with

$$s_x = -(2L_x - L_0 - L_1)/(L_0 - L_1), \tag{S8}$$
$$s_y = (2L_y - L_0 - L_1)/(L_0 - L_1), \tag{S9}$$
$$s_z = (2L_z - L_0 - L_1)/(L_0 - L_1). \tag{S10}$$

The two-qubit state tomography technique is based on the single-qubit state tomography method. The key point is to apply one or two additional transfer pulses (RF/MW pulses, see concrete sequences in Ref. [14]) to divide the full 4×4 density matrix of two qubits into several 2×2 reduced density matrices. Then, we can in turn obtain the real and imaginary parts of each element of the density matrix by implementing the single-qubit state tomography in each working transition (see Refs. [13, 14]).

E. Phase factor of the QFI

In the main text, the following formulas are assumed to describe the QFI of the electron qubit only subject to the ^{14}N or ^{13}C dissipative channel:

$$\mathcal{Q}_{\rm n}(t) = 1 - \sin^2\phi_1 \sin^2(A_{\rm n}^{\parallel}t/2 + \varphi_1/2), \tag{S11}$$
$$\mathcal{Q}_{\rm c}(t) = 1 - \sin^2\phi_2 \sin^2(A_{\rm c}^{\parallel}t/2 + \varphi_2/2). \tag{S12}$$

In the ideal case, the phase factors, φ_1 and φ_2 should be zero, which refers to a perfect initial state of the electron spin state. In our experiments, a single microwave $\pi/2$ pulse is used to create the target state, $|+\rangle_{\rm e} = (|0\rangle_{\rm e} + |1\rangle_{\rm e})/\sqrt{2}$. If the ^{14}N and ^{13}C nuclear spins are at their eigenstates, a resonant $\pi/2$ pulse can prepare the electron spin state $|+\rangle_{\rm e}$ perfectly. However, if the nuclear spin is at a superposition state (e.g., $(|\uparrow\rangle_{\rm c} + |\downarrow\rangle_{\rm c})/\sqrt{2}$), a single microwave $\pi/2$ pulse cannot be resonant with the two transition frequencies simultaneously ($|\uparrow\rangle_{\rm c}$ and $|\downarrow\rangle_{\rm c}$ subspaces), and the prepared state is only close to the target one. Therefore, the QFI starts at a value of less than 1 and oscillates at a frequency determined by the coupling strength. The QFI flow is then fitted with a non-zero phase factor. We use a relative strong microwave driving (with a Rabi frequency $\sim$ 24 MHz) to suppress this imperfection (off-resonant driving). The phase factors extracted from the experimental data are $\sim \pi/60$ and $\sim \pi/3$ for the ^{14}N and ^{13}C nuclear spins, respectively.

F. QFI envelope induced by the spin bath

To quantitatively describe the influence of the spin bath on the dynamics of the quantum open system, we measure the long-term QFI of the NV electron spin, when all the controllable channels (12.8 MHz ^{13}C and 2.16 MHz ^{14}N) are turned off after polarizing by a short laser [see Fig. S4(b)]. In Fig. S4(a) and S4(b), we find that the coherence and QFI decay non-monotonously, with a 0.45 MHz oscillation. We attribute this oscillation to the effects of the partially polarized ^{13}C nuclear spin, of which the hyperfine coupling strength is about 0.4 MHz, and the quantization axis is not the same as the NV electron spin's [10]. Therefore, we can only regard the 0.4 MHz ^{13}C nuclear spin as an uncontrollable quantum channel and fit the experimental results using the formula

$$\mathcal{Q}_{\rm R}(t) = \exp[-(t/\widetilde{T}_2^*)^{\alpha}][1 - \sin^2\phi_0 \sin^2(A_{\rm c0}^{\parallel}t/2)], \tag{S13}$$

with $\alpha = 0.64$, $\widetilde{T}_2^* \simeq 705$ ns, $\phi_0 = 0.37\pi$, and $A_{\rm c0}^{\parallel} = 0.45$ MHz. It should be noted that within the time scale of

our experiments (0–600 ns), the dissipative channel of the 0.4 MHz ^{13}C nuclear spin behaves Markovian, which has been included in the Markovian channel of the spin bath [see Fig. S4(b)].

G. Data processing

The measurements in our experiments are repeated at least 4×10^5 times to obtain a good signal-to-noise ratio. In the first experiment, each data point of the QFI is calculated from the measured photon counts (L_x, L_y, L_z, L_0, and L_1) using Eqs. (S8–S10). The QFI data is then used to calculate the QFI flow. As the step time of our QFI measurement is less than 8 ns, during which the change of QFI is very small and could be buried by the random fluctuation of adjacent data points. To combat this problem, we smooth the QFI data by averaging 5 adjacent points in the calculation of QFI flow. In the second experiment, each data point of the QFI is obtained from the full 4×4 density matrix of two qubits. The final density matrix is extracted from the measured photon counts, according to the two-qubit state tomography technique, and optimized by a maximum likelihood estimation (MLE) to reduce measurement errors.

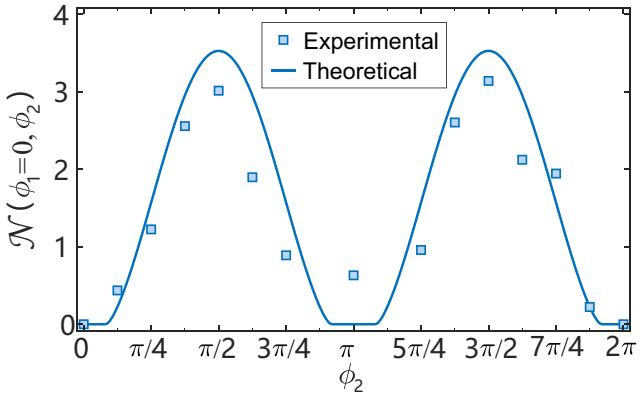

FIG. S5. The non-Markovianity measure $\mathcal{N}(0,\phi_2) \equiv N(t\to\infty,0,\phi_2)$ for different parameters of the ^{13}C dissipative channel, when the ^{14}N channel is closed. The experimental data are obtained for a relatively long evolution time $t = 600$ ns. The solid lines are for the numerical simulations using experimental parameters.

[1] S. L. Braunstein and C. M. Caves, "Statistical distance and the geometry of quantum states," Phys. Rev. Lett. **72**, 3439–3443 (1994).

[2] Géza Tóth, "Multipartite entanglement and high-precision metrology," Phys. Rev. A **85**, 022322 (2012).

[3] Luca Pezzé and Augusto Smerzi, "Entanglement, nonlinear dynamics, and the heisenberg limit," Phys. Rev. Lett. **102**, 100401 (2009).

[4] Y.-R. Zhang, Y. Zeng, H. Fan, J. Q. You, and F. Nori, "Characterization of topological states via dual multipartite entanglement," Phys. Rev. Lett. **120**, 250501 (2018).

[5] X.-M. Lu, X. G. Wang, and C. P. Sun, "Quantum Fisher information flow and non-Markovian processes of open systems," Phys. Rev. A **82**, 042103 (2010).

[6] H.-P. Breuer, E.-M. Laine, J. Piilo, and B. Vacchini, "Colloquium: Non-Markovian dynamics in open quantum systems," Rev. Mod. Phys. **88**, 021002 (2016).

[7] R. Ángel, F. H. Susana, and B. P. Martin, "Quantum non-Markovianity: Characterization, quantification and detection," Rep. Prog. Phys. **77**, 094001 (2014).

[8] L. Marseglia, J. P. Hadden, A. C. Stanley-Clarke, J. P. Harrison, B. Patton, Y.-L. D. Ho, B. Naydenov, F. Jelezko, J. Meijer, P. R. Dolan, J. M. Smith, J. G. Rarity, and J. L. O'Brien, "Nanofabricated solid immersion lenses registered to single emitters in diamond," Appl. Phys. Lett. **98**, 133107 (2011).

[9] B. Smeltzer, L. Childress, and A. Gali, "^{13}C hyperfine interactions in the nitrogen-vacancy centre in diamond," New J. Phys. **13**, 025021 (2011).

[10] A. Dréau, J.-R. Maze, M. Lesik, J.-F. Roch, and V. Jacques, "High-resolution spectroscopy of single NV defects coupled with nearby ^{13}C nuclear spins in diamond," Phys. Rev. B **85**, 134107 (2012).

[11] A. Jarmola, V. M. Acosta, K. Jensen, S. Chemerisov, and D. Budker, "Temperature- and magnetic-field-dependent longitudinal spin relaxation in Nitrogen-vacancy ensembles in diamond," Phys. Rev. Lett. **108**, 197601 (2012).

[12] P. C. Maurer, G. Kucsko, C. Latta, L. Jiang, N. Y. Yao, S. D. Bennett, F. Pastawski, D. Hunger, N. Chisholm, M. Markham, D. J. Twitchen, J. I. Cirac, and M. D. Lukin, "Room-temperature quantum bit memory exceeding one second," Science **336**, 1283 (2012).

[13] T. van der Sar, Z. H. Wang, M. S. Blok, H Bernien, T. H. Taminiau, D. M. Toyli, D. A. Lidar, D. D. Awschalom, R Hanson, and V. V. Dobrovitski, "Decoherence-protected quantum gates for a hybrid solid-state spin register," Nature **484**, 82–86 (2012).

[14] G. Q. Liu, H. C. Po, J. Du, R. B. Liu, and X. Y. Pan, "Noise-resilient quantum evolution steered by dynamical decoupling," Nat. Commun. **4**, 2254 (2013).